



Mathematical modelling of direct borohydride fuel cells

A.A. Shah^{a,*}, R. Singh^b, C. Ponce de León^c, R.G. Wills^c, F.C. Walsh^c

^a School of Engineering, University of Warwick, Coventry CV4 7AL, UK

^b Institute for Integrated Energy Systems, University of Victoria, British Columbia V8W 3P6, Canada

^c Faculty of Engineering and the Environment, University of Southampton, Southampton SO17 1BJ, UK

HIGHLIGHTS

- The first detailed model of a direct-borohydride/oxygen fuel cell is developed.
- The performance is simulated and compared to experimental results.
- The performance on Pt and Ni anodes is simulated and the differences are explained.
- Extensions to the model are outlined.
- Key property values missing from the open literature are highlighted.

ARTICLE INFO

Article history:

Received 1 June 2012

Received in revised form

25 July 2012

Accepted 28 July 2012

Available online 6 August 2012

Keywords:

Direct borohydride fuel cell

Mathematical model

Mixed potential

Polarization

Performance

ABSTRACT

A detailed mathematical model for the direct borohydride/O₂ fuel cell is developed. The activation polarizations, mass-transport limitations and resistances to charge transport in each component of the cell are explicitly incorporated. The anode kinetic mechanism is based on direct borohydride oxidation, borohydride hydrolysis and the full Tafel–Volmer–Heyrovsky mechanism for hydrogen evolution and oxidation. The mixed potential at the anode is calculated using the mixed-potential theory. The model results are compared to experimental data across a range of operating conditions and component properties, including the reactant concentrations, the anolyte flow rate, the ionomer volume fractions and the membrane/ionomer conductivity. A good qualitative fit to the experimental data is demonstrated. In order to gain insight into the anode reaction mechanism, the performance on both Pt and Ni anodes is simulated and compared to experimental observations. A detailed analysis of the results provides an explanation for the different performance on these catalysts.

© 2012 Elsevier B.V. All rights reserved.

1. Introduction

Direct hydrogen fuel cells have the potential to provide clean and sustainable power for a broad range of applications, from automotive propulsion to portable consumer electronics [1]. Cost effective and safe methods for sourcing, storing and handling hydrogen are key to the mass commercialisation of hydrogen fuel cell technology. Widespread adoption also requires radical changes to existing fuel infrastructures. In order to alleviate many of the problems related to the introduction of a hydrogen infrastructure, reformers can be employed to convert a hydrocarbon liquid fuel to hydrogen, but this introduces additional engineering complications and increases the costs, space requirements and weights of the fuel-cell power systems.

Replacing hydrogen with methanol is a potential solution to the aforementioned problems. Direct-methanol fuel cells (DMFC), on the other hand, suffer from methanol crossover and low open-circuit voltages (OCVs) [2], in part due to the inefficient anodic oxidation of methanol. The problems arising from the use of liquid methanol have led to a search for alternative hydrogen-carrier compounds, of which borohydride compounds are a prominent example [3]. A cell that utilizes a borohydride compound (usually sodium borohydride) as the fuel, a cation or anion exchange membrane and O₂ [4] or H₂O₂ [5] (in anaerobic environments) as an oxidant is termed a direct borohydride fuel cell (DBFC). A Schematic of the O₂ DBFC is shown in Figure 1.

DBFCs are characterized by their high OCVs (considerably higher OCVs than all other fuel cell technologies), low operating temperatures and high power densities [6,7]. These characteristics, in combination with their environmentally friendly by-products of reaction, have generated considerable interest in DBFCs. The cell power density and charge efficiency of DBFCs are strongly

* Corresponding author. Tel.: +44 24 761 51676; fax: +44 24 76 418922.

E-mail address: Akeel.Shah@warwick.ac.uk (A.A. Shah).

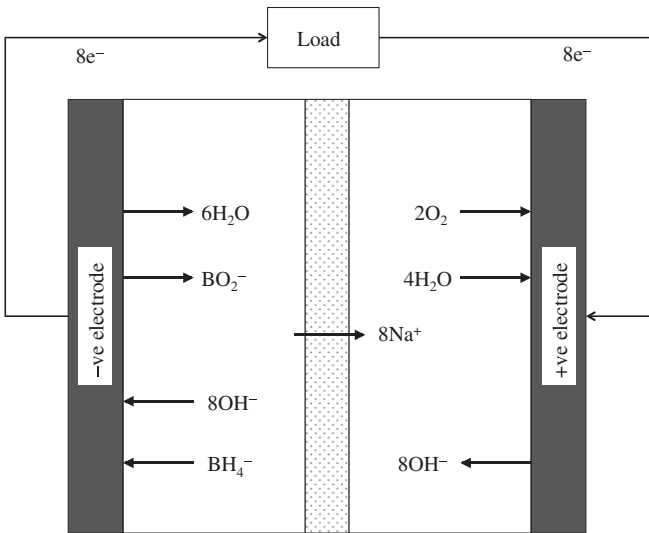


Fig. 1. Schematic of a direct borohydride fuel cell operating with O_2 as the oxidant.

influenced by the choice of anode catalyst. A complete (or close to complete) eight e^- anodic oxidation is feasible with Au and Ag electrodes [3,8,9], while Pt appears to liberate up to only four electrons [10]. One of the most appealing aspects of DBFCs is the ease with which the BH_4^- ions can be oxidised on non-precious materials such as Ni and Pd, as well as many common alloys used for hydrogen storage [7,10].

Amongst other factors, the electrode and support materials [7,10], the reactant concentrations [11,12], the PTFE/Nafion binder content in the anode [13,14], the operating conditions [11,15], the fuel pH [13], the diffusion layer properties [16], the membrane [7], the electrode structure [17] and the cell/stack design [7,10,18] influence the power density and efficiency of DBFCs. The anode materials, anolyte composition, membrane and operating conditions have a major effect on the evolution of H_2 , which is an inherent feature of DBFCs. H_2 evolution, which can occur via at least two pathways, lowers the charge efficiency of the cell, inhibits reactant transport and poses safety concerns. The cathode performance is also not trivial. It has been demonstrated in several studies that the cathode polarisation is a major source of voltage loss [4,12,19], partly due to the establishment of a mixed potential resulting from borohydride crossover [20,21].

The performance of current DBFCs is highly encouraging, but further improvement and optimization are required. Amongst other considerations, there is ongoing research into the anode design, particularly with respect to suppressing H_2 evolution, examining and understanding the voltage losses under different design and operating conditions, and further understanding the anode and cathode reactions. In contrast to other types of fuel cells [22], there have been very few attempts to model DBFCs mathematically [23]. Verma and Basu [24] developed a highly simplified steady-state model of an O_2 DBFC to predict the cell voltage at a given current density. Activation overpotentials were estimated by inverting Tafel relationships and oxygen diffusion across a gas diffusion layer was incorporated by linearising Fick's law. Diffusion in the catalyst layer, which is the overwhelming source of mass transfer limitations, was neglected. Ohmic resistances were modelled by estimating an overall resistance from experimental data. To obtain a reasonable qualitative fit to experimental data, an ad hoc term representing the concentration polarisation in the anode was required. Sanli et al. [25] developed a series of similar models for a BH_4^-/H_2O_2 DBFC, ignoring mass, charge and heat transport. Concentration overpotentials were derived by including

reactant concentrations inside a Tafel expression and by introducing a limiting current density. The ohmic losses were characterised by a constant resistance, estimated experimentally along with the reaction constants and the OCV. Only by including the cathode explicitly was a reasonable fit to the data possible. As in Ref. [24], a narrow range of current density was considered (up to only 0.02 A cm^{-2}). Models of this level of simplicity can provide a means for monitoring performance but lack sufficient physical detail for enhancing fundamental understanding of DBFC operation and for improving designs. Material properties, solution compositions, the complex reaction kinetics and the operating conditions are known to exert a strong influence on the performance of DBFCs. Incorporating these aspects of DBFC design and operation is key to developing effective modelling and simulation tools.

In this paper, a physics-based model for an O_2 DBFC is developed. The model incorporates the main factors affecting the cell voltage. Borohydride oxidation, hydrolysis and hydrogen evolution/oxidation are included in the anode mechanism. The full Tafel–Volmer–Heyrovsky mechanism is employed for the hydrogen evolution/oxidation reactions, together with competitive adsorption of H and BH_4^- . The mixed potential theory is employed to estimate the anode polarization. The predicted trends with respect to variations in key variables, including the reactant concentrations, the anolyte flow rate, the ionomer volume fractions and the membrane/ionomer properties, are then compared to experimental observations (from the open literature) and the results are analyzed and explained. The performance on a Pt/C anode and the performance on Ni anode are also simulated and compared. Explanations for the differences observed in the simulations (and in experiments) are proposed.

2. Mathematical model

Given a constant applied current density j_{applied} , the output of the model will be a value for the cell voltage. By varying j_{applied} , a polarization curve can be simulated. The cell voltage is calculated by subtracting the activation, ohmic and concentration polarisations from the OCV (at which the net current flow from the anode to the cathode is zero). The concentration polarisations are included in the activation polarisations by explicitly including the mass transfer resistances.

In the model developed, the cathode is considered to consist of a Pt/C and PTFE catalyst layer pasted onto a gas diffusion layer (GDL), in the form of a graphite paper. The anode consists of either Pt/C or Ni mixed with PTFE pasted onto a Ni foam. The electrodes are separated by a Nafion membrane. A schematic of the MEA is presented in Fig. 2. The cell is similar to that developed by Li et al. in Ref. [14] and where parameter values are available from that paper, they will be used in this study. It is important to point out that the focus of this study is to develop a physics-based framework for modelling DBFC and to validate the approach by capturing qualitative trends, rather than quantitatively fitting to experimental data. There is no loss of generality in this approach; once suitable data is available, together with all material properties, a quantitative fit would be straightforward to achieve.

Several simplifying assumptions were adopted in the development of the model. The main assumptions and their justifications are listed below.

1. The reactant concentrations are assumed to be spatially homogeneous in each component, although the main transport limitations are incorporated.
2. The generated H_2 gas forms gas bubbles, which travel at a different velocity from the bulk anolyte velocity; departures are induced by drag forces, equal in magnitude to the buoyancy

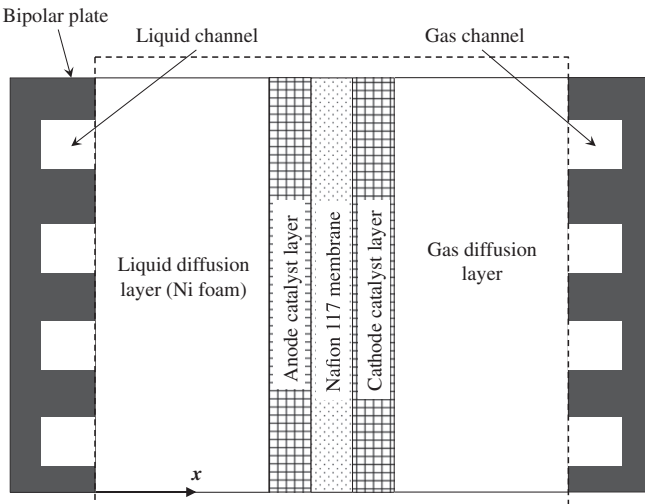


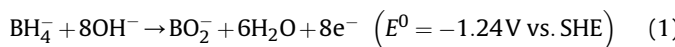
Fig. 2. Schematic of the cell modelled (the components enclosed in the dotted line).

force exerted on the bubbles [26]. Incorporation of these effects is not attempted in this paper. The H₂ is treated as either a dissolved or an adsorbed species.

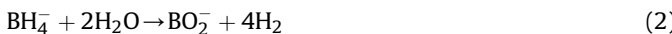
3. The reaction mechanism in the anode is dependent on the catalysts and at present is poorly understood. Therefore, a general mechanism that accounts for direct borohydride oxidation, hydrogen evolution and hydrogen oxidation is adopted (details are provided in the next subsection).

2.1. Reaction mechanisms and reaction rates

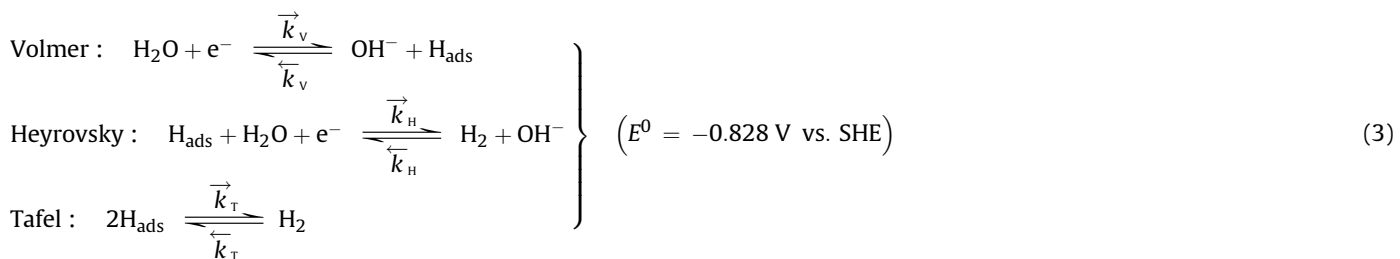
Activation losses or polarizations are a consequence of the energy barriers associated with the charge transfer reactions occurring at an electrode. In other words, a portion of the voltage generated is consumed in transmitting electrons to or from the electrode. At the anode, borohydride ions BH₄⁻ are (ideally) oxidized directly on the electrode. This process can theoretically liberate eight electrons [6,7]:



The borohydride fuel, however, tends to hydrolyze rapidly on most candidate electrocatalysts, leading to the formation of H₂ [6,7]:



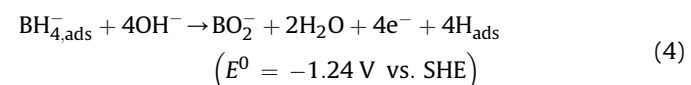
This competitive reaction reduces the charge efficiency of the cell and the accompanying formation of H₂ leads to a deterioration in cell performance due to the presence of H₂ bubbles in the anolyte (H₂ molecules hinder ion movement). Reaction (2) is accompanied by a second pathway to H₂ evolution, namely the reduction of water:



Mechanism (3) is the full Tafel–Volmer–Heyrovsky mechanism, in which H_{ads} represents an adsorbed adatom of hydrogen. The \overrightarrow{k}_v and \overleftarrow{k}_h are forward and backward reaction rate constants, respectively. Water reduction is thermodynamically favoured at the formal potential for borohydride oxidation (1), suggesting that a mixed potential is established at the anode. Indeed, the observed anode potentials are significantly more positive than -1.24 V vs. SHE and more negative than -0.828 V vs. SHE [7].

There is evidence that Au, Ag and some hydrogen storage alloys are capable of supporting a full anodic oxidation of the borohydride under certain conditions (either due to inactivity towards hydrolysis or possible H₂ adsorption followed by oxidation), while Pt and Ni can generally support only a four-electron oxidation [8,27–29]. The oxidation of certain intermediates of hydrolysis, such as BH₃(OH)⁻, is also possible. From the early work by Bard and co-workers [30,31], the initial step on Au is thought to be an electron transfer followed by a rapid decomposition of a radical and a further electron transfer step, i.e., an electrochemical–chemical–electrochemical sequence. The intermediates (e.g., monoborane) undergo further reactions to liberate a six (eight in total) electrons, though the precise nature of these reactions is still subject to speculation. Chatenet et al. [8] studied the direct oxidation of NaBH₄ on Ag and Au in concentrated NaOH solutions using linear and cyclic voltammetry. They found that BH₄⁻ electro-oxidation depends strongly on the ratio of [BH₄⁻] to [OH⁻]. For a low BH₄⁻ concentrations, the rate of chemical hydrolysis of BH₄⁻ was negligible but at low ratios of [BH₄⁻] to [OH⁻], borohydride oxidation was limited and the borohydride ions spontaneously hydrolyzed to BH₃(OH)⁻, which undergoes oxidation at low potentials. There are, however, a number of apparently contradictory results and conclusions in the literature, in part due to the different conditions and experimental procedures used (such as full cell vs. rotating disk electrode). For example, the results of Li et al. [19] suggest that full anodic oxidation is possible on Pt under certain conditions. For a comprehensive discussion on the anode reactions on different catalysts, the reader is referred to the recent review by Merino-Jiménez et al. [23].

Based on H₂ evolution data for a range of anode catalysts, Wang et al. [32,33] proposed a reaction mechanism consisting of: (a) a four-electron direct borohydride oxidation involving H₂ evolution (reaction (4)), and (b) separate hydrogen evolution/oxidation via reaction (3):



Reaction (4) is a special case of the reaction proposed by Li et al. [19] in which four (of a possible eight) electrons are transferred and the H₂ is assumed to be adsorbed. While this mechanism may ignore the possible role of intermediates such as BH₃(OH)⁻, it provides a framework for explaining some of the observed effects, such as a mixed anode potential. The model developed in this paper is,

therefore, based on the mechanism proposed by Wang et al. [32,33], with a preliminary step of BH_4^- adsorption, as proposed by Chatenet et al. [8] (but not by Wang et al.):



The rate of the Tafel step in mechanism (3) and the rate of reaction (5) can be expressed as follows:

$$\begin{aligned} r_T &= \vec{k}_T \theta_{\text{Pt}}^2 a_{\text{H}_2} - \vec{k}_T \theta_{\text{H}}^2 \\ r_{\text{BH}} &= \vec{k}_{\text{BH}} \theta_{\text{Pt}} a_{\text{BH}_4^-} - \vec{k}_{\text{BH}} \theta_{\text{BH}_4^-} \end{aligned} \quad (6)$$

respectively, in which $a_{\text{BH}_4^-}$ and a_{H_2} are the surface activities of BH_4^- and H_2 , and $\theta_{\text{BH}_4^-}$, θ_{H} and θ_{Pt} are the catalyst-surface coverages of BH_4^- , the H adatoms and free catalyst sites, respectively. The \vec{k}_i and \vec{k}_i are again the forward and backward rate constants for the two reactions. As a simplification, the activity (pressure) of hydrogen in equation (6) is assumed to be unity.

The Butler–Volmer equation [34] can be used to approximate the transfer current density associated with reaction (4). Cheng and Scott showed that the transfer current density is first-order with respect to OH^- [35]. Since the concentration of water in the anolyte is much higher than the concentration of borohydride ions and sodium hydroxide, it is reasonable to assume a unit activity for water. The dependence on the BO_2^- concentration is also neglected since the reverse of reaction (4) is exponentially small at the mixed anode potential. Accordingly:

$$\begin{aligned} j_{\text{BH}} &= j_{\text{BH},\text{ref}} \theta_{\text{BH}_4^-} \left(\frac{c_{\text{OH}^-}}{c_{\text{OH}^-}^{\text{ref}}} \right) \left\{ \exp\left(\frac{a_1 n_a F \eta_{\text{BH}}}{RT}\right) \right. \\ &\quad \left. - \exp\left(\frac{-(1-a_1)n_a F \eta_{\text{BH}}}{RT}\right) \right\} \end{aligned} \quad (7)$$

where j_{BH} is the borohydride oxidation current density; $j_{\text{BH},\text{ref}}$ is the reference exchange current density associated with the borohydride oxidation reaction; c_{OH^-} is the concentration of OH^- at the electrode catalyst surface and $c_{\text{OH}^-}^{\text{ref}}$ is the corresponding reference concentration (at which $j_{\text{BH}} = j_{\text{BH},\text{ref}}$); η_{BH} is the overpotential; R is the universal gas constant; T is the cell temperature; F is Faraday's constant; n_a is the number of electrons transferred (four); and a_1 is the charge transfer coefficient. The overpotential is given by:

$$\eta_{\text{BH}} = \phi_s - \phi_e - E_{\text{BH}}^{\text{eq}} \quad (8)$$

in which $E_{\text{BH}}^{\text{eq}}$ is the equilibrium potential for reaction (4), ϕ_s is the electronic potential and ϕ_e is the ionic potential.

The transfer current density associated with the water reduction reaction (3) is estimated using a generalized form of the Butler–Volmer equations for the Volmer and Heyrovsky steps [36–40], assuming a unit water activity and assuming that the sodium hydroxide is not limiting:

$$j_V = F \left\{ \vec{k}_V \theta_{\text{H}} \exp\left(\frac{a_2 F \eta_{\text{H}}}{RT}\right) - \vec{k}_V \theta_{\text{Pt}} \exp\left(\frac{-(1-a_2)F \eta_{\text{H}}}{RT}\right) \right\} \quad (9)$$

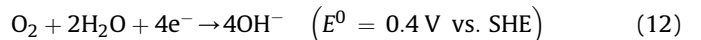
$$j_{\text{H}} = F \left\{ \vec{k}_{\text{H}} \theta_{\text{Pt}} \exp\left(\frac{a_2 F \eta_{\text{H}}}{RT}\right) - \vec{k}_{\text{H}} \theta_{\text{H}} \exp\left(\frac{-(1-a_2)F \eta_{\text{H}}}{RT}\right) \right\} \quad (10)$$

where η_{H} is the overpotential and a_2 is the charge transfer coefficient. A unit hydrogen activity is again assumed in equation (10). The overpotential is defined as:

$$\eta_{\text{H}} = \phi_s - \phi_e - E_{\text{H}}^{\text{eq}} \quad (11)$$

where E_{H}^{eq} is the equilibrium potential for reaction (3).

The reaction in the air-breathing cathode is represented as follows [6,7]:



The cathode transfer current density can be expressed as follows, making the reasonable approximation of a unit water activity:

$$j_{\text{O}_2} = j_{\text{O}_2,\text{ref}} \left(\frac{c_{\text{O}_2}}{c_{\text{O}_2}^{\text{ref}}} \right) \left\{ \exp\left(\frac{a_3 n_c F \eta_c}{RT}\right) - \exp\left(\frac{-(1-a_3)n_c F \eta_c}{RT}\right) \right\} \quad (13)$$

where $j_{\text{O}_2,\text{ref}}$ is the exchange current density associated with reaction (12); c_{O_2} is the oxygen concentration at the reaction sites (platinum surfaces) and $c_{\text{O}_2}^{\text{ref}}$ is the corresponding reference concentration; n_c is the number of electrons transferred; and η_c is the cathode overpotential. The dependence on OH^- is neglected since reaction (12) is irreversible and the OH^- ions are not limiting. The cathode overpotential is defined as:

$$\eta_c = \phi_s - \phi_e - E_c^{\text{eq}} \quad (14)$$

where E_c^{eq} is the equilibrium potential for reaction (12).

2.2. Activation overpotentials and anode polarization

For a non-zero constant applied current density, j_{applied} , the cathode overpotential is obtained by inverting the following equation, which relates the transfer current density, j_{O_2} , defined in equation (13), to j_{applied} :

$$r_c j_{\text{O}_2} = j_{\text{applied}} \quad (15)$$

where the quantity $r_c = A_a^{\text{cath}}/A_g$ is the roughness factor of the cathode; A_a^{cath} is the active surface area for reaction in the cathode and A_g is the geometrical surface area of both electrodes (the exchange current density is per unit area of the active catalyst, while the applied current density is per unit geometric area of the electrode). An expression for the surface oxygen concentration is derived in the next subsection.

The potential at the anode is a mixed potential [41] due to the simultaneous occurrence of the borohydride oxidation and water reduction reactions (4) and (3). Under the condition of a zero current density, these reactions are not at equilibrium since the mixed potential E_{mixed}^0 lies between the equilibrium potentials for reactions (4) and (3), with the anodic branch of (4) and the cathodic branch of (3) dominating, i.e., there is a balance between the electrons released in reaction (4) and electrons consumed in reaction (3). Mathematically, this can be expressed as follows, using equations (7), (9) and (10) with $a_1 = a_2 = 0.5$ [41]:

$$\begin{aligned} j_{\text{BH},\text{ref}} \theta_{\text{BH}_4^-} \left(\frac{c_{\text{OH}^-}}{c_{\text{OH}^-}^{\text{ref}}} \right) \exp\left(\frac{n_a F (E_{\text{mixed}}^0 - E_{\text{BH}}^{\text{eq}})}{2RT}\right) \\ - F (\vec{k}_V \theta_{\text{H}} + \vec{k}_{\text{H}} \theta_{\text{Pt}}) \exp\left(\frac{-F (E_{\text{mixed}}^0 - E_{\text{H}}^{\text{eq}})}{2RT}\right) = 0 \end{aligned} \quad (16)$$

Given values for the reactant concentrations and for $E_{\text{BH}}^{\text{eq}}$ and E_{H}^{eq} , equation (16) can be solved for the *mixed anode open-circuit potential* E_{mixed}^0 (i.e., the difference between the electronic and ionic potentials, $\phi_s - \phi_e$, at zero current density). For a non-zero constant applied current density, j_{applied} , conservation of electronic charge demands that:

$$r_a(j_{\text{BH}} + j_V + j_H) = j_{\text{applied}} \quad (17)$$

where the quantity $r_a = A_a^{\text{an}}/A_g$ is the roughness factor of the anode. Therefore:

$$\begin{aligned} \frac{j_{\text{applied}}}{r_a} &= j_{\text{BH,ref}} \theta_{\text{BH}_4} \left(\frac{c_{\text{OH}^-}}{c_{\text{OH}^-}^{\text{ref}}} \right) \exp \left(\frac{n_a F}{2RT} (E_{\text{mixed}} - E_{\text{BH}}^{\text{eq}}) \right) \\ &\quad + F \left\{ \overleftarrow{k}_V \theta_H \exp \left(\frac{F}{2RT} (E_{\text{mixed}} - E_{\text{H}}^{\text{eq}}) \right) \right. \\ &\quad \left. - \overrightarrow{k}_V \theta_P \exp \left(- \frac{F}{2RT} (E_{\text{mixed}} - E_{\text{H}}^{\text{eq}}) \right) \right\} \\ &\quad + F \left\{ \overleftarrow{k}_H \theta_P \exp \left(\frac{F}{2RT} (E_{\text{mixed}} - E_{\text{H}}^{\text{eq}}) \right) \right. \\ &\quad \left. - \overrightarrow{k}_H \theta_H \exp \left(- \frac{F}{2RT} (E_{\text{mixed}} - E_{\text{H}}^{\text{eq}}) \right) \right\} \end{aligned} \quad (18)$$

Equation (18) can be solved for the *mixed anode potential* E_{mixed} , which is the difference between the electronic and ionic potentials pertaining to a non-zero current density. The polarization of the anode, η_{mixed} is calculated from the following equation:

$$\eta_{\text{mixed}} = E_{\text{mixed}} - E_{\text{mixed}}^0 \quad (19)$$

2.3. Mass balances

Calculation of the activation losses in both the anode and cathode requires estimates of the reactant concentrations at the electrode surfaces, where the reactions take place. The DBFC in Ref. [4] utilized porous electrodes for both the anode and cathode. In the model developed, the anolyte is circulated through the anode at a constant volumetric flow rate ω . A liquid diffusion layer (Ni foam) is assumed to separate the anode catalyst layer (ACL) and the anolyte inlet and outlet (a common design). It is assumed that the electric current enters uniformly along bipolar plate surfaces, i.e., in the through-plane direction x in Fig. 2.

The concentrations of the active species in the anode (comprising the catalyst layer and Ni foam) are derived from a mass balance based on the circulation of the anolyte together with reactant consumption or generation. At practical flow rates, diffusive transport in the anode is negligible in comparison to convective transport, except within mass-transfer boundary layers. To model the resistance to mass-transfer between the bulk region (pore space) and the reaction sites (catalyst surfaces), a Nernst diffusion boundary layer [41] is introduced. The bulk anolyte solution is considered well mixed in the catalyst layer and Ni foam, leading to uniform bulk species concentration values that are valid in both regions. At steady state, molar balances for the species $i = \text{BH}_4^-, \text{BO}_2^-, \text{OH}^-$ in the bulk region can be written as follows:

$$\omega \left(c_i^{\text{inlet}} - c_i^{\text{bulk}} \right) - \frac{A_a^{\text{an}} D_i^{\text{eff}}}{\delta_i} \left(c_i^{\text{bulk}} - c_i \right) = 0 \quad (20)$$

where A_a^{an} is the surface area to which the reactants diffuse through the boundary layer (the active surface area for reaction in the anode); δ_i is the Nernst boundary layer thickness for species i ; c_i^{inlet} , c_i^{bulk} and c_i are the inlet, bulk (in the catalyst layer and Ni foam) and catalyst surface concentrations of species i , respectively; and D_i^{eff} is

the effective diffusion coefficient of species i in solution in the catalyst layer. D_i^{eff} can be approximated using the Bruggeman correction [42]: $D_i^{\text{eff}} = \varepsilon_{\text{acl}}^{3/2} D_i$, where ε_{acl} is the porosity of the ACL and D_i is the free-space diffusion coefficient in solution. The steady state molar balances for species $i = \text{BO}_2^-, \text{OH}^-$ in the diffuse layer can be written as follows:

$$\frac{A_a^{\text{an}} D_i^{\text{eff}}}{\delta_i} \left(c_i^{\text{bulk}} - c_i \right) - \left(\frac{\nu_i A_a^{\text{an}} j_{\text{BH}}}{n_a F} + \frac{(\mu_i j_V + \pi_i j_H) A_a^{\text{an}}}{F} \right) = 0 \quad (21)$$

in which ν_i is the stoichiometric coefficient of species i in reaction (4), and μ_i and π_i are the stoichiometric coefficients of species i in the Volmer and Heyrovsky steps (3), respectively (taken as positive if the species is a reactant and negative if the species is a product). Eliminating the bulk concentration in equations (20) and (21) yields expressions for the surface and bulk concentrations of species $i = \text{BO}_2^-, \text{OH}^-$:

$$\begin{aligned} c_i &= c_i^{\text{inlet}} - \left(\frac{A_a^{\text{an}}}{\omega} + \frac{\delta_i}{D_i^{\text{eff}}} \right) \left(\frac{\nu_i j_{\text{BH}}}{n_a F} + \frac{\mu_i j_V + \pi_i j_H}{F} \right) \\ c_i^{\text{bulk}} &= c_i^{\text{inlet}} - \frac{A_a^{\text{an}}}{\omega F} \left(\frac{\nu_i j_{\text{BH}}}{n_a} + \mu_i j_V + \pi_i j_H \right) \end{aligned} \quad (22)$$

The surface concentration of BH_4^- is calculated from a steady-state balance that takes into account diffusion to the reaction sites and adsorption and desorption, the rates of which are given in equation (6). The activity of BH_4^- in the latter equation is approximated by the ratio of the BH_4^- surface concentration to the inlet concentration, $c_{\text{BH}_4^-}^{\text{inlet}}$. The mass balance therefore reads:

$$\begin{aligned} \frac{A_a^{\text{an}} D_{\text{BH}_4^-}^{\text{eff}}}{\delta_{\text{BH}_4^-}} \left(c_{\text{BH}_4^-}^{\text{bulk}} - c_{\text{BH}_4^-} \right) &= A_a^{\text{an}} r_{\text{BH}} \\ &= A_a^{\text{an}} \left(\hat{k}_{\text{BH}} \theta_P c_{\text{BH}_4^-} - \overleftarrow{k}_{\text{BH}} \theta_{\text{BH}_4^-} \right) \end{aligned} \quad (23)$$

which is combined with equation (20). In equation (23), the modified reaction constant $\hat{k}_{\text{BH}} = \overrightarrow{k}_{\text{BH}}/c_{\text{BH}_4^-}^{\text{inlet}}$ has been introduced to simplify notation. Equations are also required for the surface coverages of hydrogen and BH_4^- , which, under steady state conditions, are given by:

$$\begin{aligned} r_T - \frac{j_V}{F} + \frac{j_H}{F} + \frac{j_{\text{BH}}}{F} &= 0 \\ r_{\text{BH}} - \frac{j_{\text{BH}}}{4F} &= 0 \end{aligned} \quad (24)$$

respectively, together with:

$$\theta_P + \theta_H + \theta_{\text{BH}_4^-} = 1 \quad (25)$$

i.e., conservation of the active catalyst sites.

There are various approaches to modelling the diffusion boundary layer thickness δ . For each oxidized/reduced species in an electrolyte-electrode structure, Chrysikopoulos et al. developed an expression for the boundary layer thickness in terms of the (mean) flow rate in a direction parallel to the layer surface [43]:

$$\delta_i = \frac{K}{\sqrt{\omega/D_i^{\text{eff}}}} \quad (26)$$

where K is a constant parameter depending on the area. The formula (26) is adopted in this paper.

The sodium ions do not participate in the anode reactions. They do, however, migrate from the anode to the cathode under the

influence of the potential gradient formed under a load. Assuming that BH_4^- , BO_2^- , OH^- and Na^+ are the only charged species in the electrolyte, the concentration of Na^+ can be calculated from the condition of electroneutrality in the bulk solution (close to the electrode surface, this condition is of course violated and a double layer develops):

$$\sum_i z_i c_i^{\text{bulk}} = 0 \quad (27)$$

where z_i is the charge number of species i . Equation (27) ensures that (in the model) Na^+ migrates to the cathode through the membrane in order to maintain charge balance in the electrodes.

The oxygen is fed to the cell through a cathode flow channel. It diffuses through a gas diffusion layer (GDL) to the cathode catalyst layer (CCL) where it reacts on the Pt/C catalyst. In such air-breathing Pt/C designs, the O_2 must diffuse through the ionomer in the catalyst layer in order to reach the reaction sites, which introduces an additional mass-transport resistance. This resistance can be incorporated by defining a boundary layer of thickness δ_{O_2} . A steady state molar balance of oxygen in the catalyst can be derived by taking into account O_2 diffusion through the GDL to the CCL, where the concentration is denoted $c_{\text{O}_2}^{\text{bulk}}$, mass transfer through the boundary layer to the catalyst surfaces, where the concentration is denoted c_{O_2} , and electrochemical reaction:

$$\begin{aligned} D_{\text{O}_2}^{\text{eff}} A_g \frac{(c_{\text{O}_2}^{\text{inlet}} - c_{\text{O}_2}^{\text{bulk}})}{l_{\text{GDL}}} - \frac{A_a^{\text{cath}} D_f^{\text{eff}}}{\delta_{\text{O}_2}} (c_{\text{O}_2}^{\text{bulk}} - c_{\text{O}_2}) &= 0 \\ \frac{A_a^{\text{cath}} D_f^{\text{eff}}}{\delta_{\text{O}_2}} (c_{\text{O}_2}^{\text{bulk}} - c_{\text{O}_2}) - \frac{j_{\text{applied}} A_g}{4F} &= 0 \end{aligned} \quad (28)$$

In equation (28): A_a^{cath} is the active surface area for reaction in the cathode (the active catalyst surface area, to which the reactants diffuse through the boundary layer); l_{GDL} is the thickness of the GDL; D^{eff} is the effective diffusion coefficient of oxygen through the ionomer film (boundary layer) and $D_{\text{O}_2}^{\text{eff}}$ is the effective diffusion coefficient of oxygen through the GDL. The effective diffusion coefficients are approximated using Bruggeman corrections [42]: $D_f^{\text{eff}} = \varepsilon_{\text{e,ccl}}^{3/2} D_f$ and $D_{\text{O}_2}^{\text{eff}} = \varepsilon_{\text{GDL}}^{3/2} D_{\text{O}_2}$, in which $\varepsilon_{\text{e,ccl}}$ is the volume fraction of ionomer in the CCL, ε_{GDL} is the porosity of the GDL, D_f is the diffusion coefficient of oxygen in the bulk ionomer and D_{O_2} is the free space diffusion coefficient of oxygen in air. Eliminating the bulk concentration in equation (28) yields an expression for the surface concentration of oxygen:

$$c_{\text{O}_2} = c_{\text{O}_2}^{\text{inlet}} - \left(\frac{l_{\text{GDL}}}{D_{\text{O}_2}^{\text{eff}}} + \frac{\delta_{\text{O}_2}}{r_c D_f^{\text{eff}}} \right) \frac{j_{\text{applied}}}{4F} \quad (29)$$

2.4. Ohmic losses

The resistances to the flow of charge in the ion-conducting and electron-conducting phases result in (additive) voltage losses, which are calculated using Ohm's law. The relevant regions are the ACL, the Ni foam, the membrane, the CCL and the cathode GDL. Both the liquid and solid phases are taken into account.

2.4.1. Ionic resistances

The ohmic drop across the membrane can be written in terms of the Na^+ conductivity of the membrane, σ_{mem} , and the applied current density (the current is purely ionic in the membrane):

$$(\Delta\phi_e)_{\text{mem}} = \frac{l_{\text{mem}}}{\sigma_{\text{mem}}} j_{\text{applied}} \quad (30)$$

in which l_{mem} is the thickness of the membrane.

Ion transport through the ionomer in the ACL (it is assumed that the ionomer is the same material, e.g. Nafion, as the membrane material, which is typically the case) takes place alongside ion transport through the anolyte solution. The ionic potential drop across the ACL must take into account these parallel processes. The drop in the ionic potential across the ACL can be calculated by considering the total ionic current density in the in the ACL, j_e , generated by the flow of charged species in the anolyte and the migration of sodium ions in the ionomer (in the through plane direction x in Fig. 2) [34]:

$$\begin{aligned} j_e &= \varepsilon_{\text{e,acl}}^{3/2} \sigma_{\text{mem}} \frac{d\phi_e}{dx} - \sum_i z_i F N_i \\ &= \varepsilon_{\text{e,acl}}^{3/2} \sigma_{\text{mem}} \frac{d\phi_e}{dx} - \sum_i z_i F v c_i^{\text{bulk}} + \sum_i z_i F D_i^{\text{eff}} \frac{dc_i^{\text{bulk}}}{dx} \\ &\quad + \sum_i z_i F \left(\frac{z_i F D_i^{\text{eff}}}{RT} \right) c_i^{\text{bulk}} \frac{d\phi_e}{dx} \\ &= \varepsilon_{\text{e,acl}}^{3/2} \sigma_{\text{mem}} \frac{d\phi_e}{dx} \\ &\quad + \sum_i z_i F \left(\frac{z_i F D_i^{\text{eff}}}{RT} \right) c_i^{\text{bulk}} \frac{d\phi_e}{dx} \equiv \sigma_{\text{e,acl}}^{\text{eff}} \frac{d\phi_e}{dx} \end{aligned} \quad (31)$$

In this equation, v is the electrolyte flow speed and N_i is the molar flux of species i , which is expressed using the Nernst–Planck equation. The effective diffusion coefficients in the ACL, D_i^{eff} , are approximated using the Bruggeman correction [42]: $D_i^{\text{eff}} = \varepsilon_{\text{acl}}^{3/2} D_i$. The conductivity of the ionomer is also based on a Bruggeman correction, using the volume fraction of ionomer in the ACL, $\varepsilon_{\text{e,acl}}$. The term $\sum_i z_i F v c_i^{\text{bulk}}$ in equation (32) is zero by virtue of the electroneutrality condition (27) and the term $\sum_i z_i F D_i^{\text{eff}} (dc_i^{\text{bulk}}/dx)$ is zero given the assumption of uniform bulk concentrations. The term $\varepsilon_{\text{acl}}^{3/2} F^2 \sum_i z_i^2 D_i c_i^{\text{bulk}} / (RT)$ is the effective conductivity of the anolyte and the overall effective ionic conductivity in the ACL, $\sigma_{\text{e,acl}}^{\text{eff}}$ is given by the sum of the effective conductivity of the anolyte and the effective conductivity of the ionomer, reflecting the parallel paths for ion conduction. Thus, the total ionic potential drop across the ACL is given by:

$$(\Delta\phi_e)_{\text{acl}} = \frac{l_{\text{acl}}}{\sigma_{\text{e,acl}}^{\text{eff}}} j_e \quad (32)$$

where l_{acl} is the thickness of the ACL.

For the ohmic drop across the CCL it is again assumed that the ionomer is the same material as the membrane material. The ohmic drop can then be written in terms of the Na^+ conductivity of the membrane and the ionic current density:

$$(\Delta\phi_e)_{\text{ccl}} = \frac{l_{\text{ccl}}}{\varepsilon_{\text{e,ccl}}^{3/2} \sigma_{\text{mem}}} j_e \quad (33)$$

in which l_{ccl} is the thickness of the CCL. Note that the effective conductivity has been approximated by $\varepsilon_{\text{e,ccl}}^{3/2} \sigma_{\text{mem}}$, using a Bruggeman correction [42].

2.4.2. Electronic resistances

To find the electronic potential drop in the ACL, the volume fractions of catalyst (either Pt or Ni in the simulations) and carbon,

$\varepsilon_{M,a}$ and $\varepsilon_{C,acl}$, respectively, and the individual conductivities of the catalyst and carbon, σ_M and σ_C , respectively, are used:

$$(\Delta\phi_s)_{acl} = \frac{l_{acl}}{\sigma_{s,acl}^{\text{eff}}} j_s = \frac{l_{acl} j_s}{\varepsilon_{M,a}^{3/2} \sigma_M + \varepsilon_{C,acl}^{3/2} \sigma_C} \quad (34)$$

where the effective conductivity $\sigma_{s,acl}^{\text{eff}}$ is given by the sum of the individual conductivities (with Bruggeman corrections), corresponding to resistances in parallel. The current density through the solid electron-conducting components is denoted j_s in equation (35).

The electronic potential drop across the CCL can be derived in a manner similar to that leading to equation (35):

$$(\Delta\phi_s)_{ccl} = \frac{l_{ccl}}{\sigma_{s,ccl}^{\text{eff}}} j_s = \frac{l_{ccl} j_s}{\varepsilon_{Pt,c}^{3/2} \sigma_{Pt} + \varepsilon_{C,ccl}^{3/2} \sigma_C} \quad (35)$$

where the effective conductivity $\sigma_{s,ccl}^{\text{eff}}$ is again given by the sum of the individual conductivities (of carbon support, with volume fraction $\varepsilon_{C,ccl}$, and platinum, with volume fraction $\varepsilon_{Pt,c}$ and conductivity σ_{Pt}).

The electronic potential drop across the Ni foam layer (in which the current is purely electronic) is given by:

$$(\Delta\phi_e)_{Ni} = \frac{l_{Ni}}{(1 - \varepsilon_{Ni})^{3/2} \sigma_{Ni}} j_{\text{applied}} \quad (36)$$

where l_{Ni} is the thickness of the Ni foam and σ_{Ni} is the conductivity of nickel. The electronic potential drop across the (carbon) cathode GDL is given by:

$$(\Delta\phi_s)_{GDL} = \frac{l_{GDL}}{(1 - \varepsilon_{GDL})^{3/2} \sigma_C} j_{\text{applied}} \quad (37)$$

The current is again purely electronic through this component. The charge balances are not explicitly incorporated. The values of j_s and j_e are instead approximated by their (formal) averages, that is, $j_s = j_e = j_{\text{applied}}/2$ in both catalyst layers. Further details are provided in the Appendix.

2.5. Calculation of the cell voltage

The cell voltage can be calculated by subtracting the ohmic losses and the activation and concentration polarizations from the OCV:

$$E_{\text{cell}} = E_{\text{cell}}^0 + \eta_{\text{mixed}} - \eta_c - (\Delta\phi_e)_{acl} - (\Delta\phi_e)_{ccl} - (\Delta\phi_e)_{mem} - (\Delta\phi_s)_{acl} - (\Delta\phi_s)_{ccl} - (\Delta\phi_s)_{Ni} - (\Delta\phi_s)_{GDL} \quad (38)$$

in which all terms except E_{cell}^0 have been defined in Sections 2.1–2.4. Note that the concentration (mass transport) polarization is incorporated in the polarizations η_{mixed} and η_c , which are dependent on the concentrations of the reactants at the electrode surfaces, which, in turn, incorporate the major mass transport resistances.

The OCV is the difference between the cathode equilibrium potential and the mixed anode open circuit potential (Section 2.2):

$$E_{\text{cell}}^0 = E_c^{\text{eq}} - E_{\text{mixed}}^0 \quad (39)$$

The individual equilibrium potentials for the reactions (4), (3) and (12) will be required to evaluate E_{cell}^0 ; they can be expressed

Table 1
Default electrochemical parameters used in the model.

Symbol	Quantity	Value	Reference
E_c^0	Standard potential of oxygen reduction	0.4 V vs. SHE	[7]
E_{BH}^0	Standard potential of borohydride oxidation	-1.24 V vs. SHE	[7]
E_H^0	Standard potential of hydrogen oxidation	-0.828 V vs. SHE	[7]
a_1	Charge transfer coefficient for reaction (4)	0.5	Assumed ^a
a_2	Charge transfer coefficients for reactions (3)	0.5	[40]
a_3	Charge transfer coefficient for reaction (12)	0.33	[46]
$j_{BH,\text{ref}}$	Reference exchange current density for reaction (4)	60 A m ⁻²	[45]
\bar{k}_V	Backward rate constant for Volmer reaction (3)	4.4×10^{-3} mol m ² s ⁻¹	[40]
\bar{k}_V	Forward rate constant for Volmer reaction (3)	4.4×10^{-4} mol m ² s ⁻¹	[40]
\bar{k}_H	Backward rate constant for Heyrovsky reaction (3)	2.4×10^{-6} mol m ² s ⁻¹	[40]
\bar{k}_H	Forward rate constant for Heyrovsky reaction (3)	2.4×10^{-5} mol m ² s ⁻¹	[40]
\bar{k}_T	Backward rate constant for Tafel reaction (3)	8.8×10^{-6} mol m ² s ⁻¹	[40]
\bar{k}_T	Forward rate constant for Tafel reaction (3)	8.8×10^{-4} mol m ² s ⁻¹	[40]
\bar{k}_{BH}	Backward rate constant for reaction (5)	0 mol m ² s ⁻¹	[8]
\bar{k}_{BH}	Forward rate constant for reaction (5)	1×10^{-5} mol m ² s ⁻¹	Fitted
$j_{O_2,\text{ref}}$	Exchange current density for reaction (12)	2.1×10^{-3} A m ⁻²	[46]
r_a	Roughness factor of the anode	100	Assumed ^a
r_c	Roughness factor of the cathode	77	[57]
$m_{Pt,c}$	Pt loading in the cathode catalyst layer	4 g m ⁻²	Assumed ^a
$m_{Pt,a}$	Pt loading in the anode catalyst layer	40 g m ⁻²	Assumed ^a

^a See Section 2.6.

using the Nernst equation [41] but as a first approximation they are taken to be equal to their standard values (Table 1).

2.6. Model parameters

The default parameter values for the model are shown in Tables 1–4. The values of the properties labelled 'Assumed' are based on the materials described below, which are typical for DBFCs.

The cathode GDL properties are based on Toray TGP-H-060 paper and the Ni foam properties are based on a commercially available foam from Sumitomo Electric. The anode catalyst

Table 2
Default operating conditions used in the model.

Symbol	Quantity	Value
T	Operating temperature	298 K
$c_{BH_4}^{\text{inlet}}$	Inlet concentration of BH_4^-	0.5 M
$c_{BO_2}^{\text{inlet}}$	Inlet concentration of BO_2^-	0.0 M
c_{OH}^{inlet}	Inlet concentration of OH^-	2.0 M
$c_{Na^+}^{\text{inlet}}$	Inlet concentration of Na^+	2.5 M
c_O^{inlet}	Inlet concentration of O_2	8.53 mol m^{-3}
$c_{O_2}^{\text{ref}}$	Reference O_2 concentration	8.53 mol m^{-3}
ω	Volumetric solution inlet flow rate	10 mL min ⁻¹

Table 3

Default structural parameters used in the model.

Symbol	Quantity	Value	Reference
ε_{GDL}	Porosity of cathode GDL (Toray)	0.73	[58]
$\varepsilon_{\text{e,ccl}}$	Ionomer volume fraction in cathode catalyst layer	0.2	[59]
$\varepsilon_{\text{e,acl}}$	Ionomer volume fraction in anode catalyst layer	0.2	Assumed ^a
ε_{Ni}	Ni foam porosity (Sumitomo Electric)	0.98	Assumed ^a
$\varepsilon_{\text{Pt,c}}$	Volume fraction of Pt in cathode catalyst layer	0.09	Assumed ^a
$\varepsilon_{\text{Pt,a}}$	Volume fraction of Pt in anode catalyst layer	0.09	Assumed ^a
$\varepsilon_{\text{C,ccl}}$	Volume fraction of carbon in the cathode catalyst layer	0.25	Assumed ^a
$\varepsilon_{\text{C,acl}}$	Volume fraction of carbon in the anode catalyst layer	0.31	Assumed ^a
l_{GDL}	Thickness of cathode GDL (Toray)	190 μm	[58]
l_{Ni}	Thickness of Ni foam (Sumitomo Electric)	1.5 mm	[58]
l_{ccl}	Thickness of cathode catalyst layer	20 μm	[57]
l_{acl}	Thickness of anode catalyst layer	200 μm	Assumed ^a
l_{mem}	Thickness of membrane (Nafion® 112/212)	50 μm	Assumed ^a
δ_{O_2}	Diffusion film thickness in the cathode	2 μm	Assumed ^a
A_{g}	Geometric surface area of the electrodes	10 cm^2	Assumed ^a

^a See Section 2.6.

properties in the tables are based on Pt/C. Values based on Ni are provided in Table 5. The film diffusion coefficient in the cathode, D_f (Table 4), is based on the diffusion coefficient through a Nafion membrane at room temperature. The reference exchange current density for borohydride anodic oxidation on Pt/C ($j_{\text{BH,ref}}$ in equation (7)) was calculated at 25 °C by Molina-Concha and Chatenet [44,45].

The reaction rate constants \vec{k}_i and \overleftarrow{k}_i for the hydrogen evolution reaction (3) on Pt (Table 1) are taken from Bai [38] (see also [39,40]), estimated at 23 °C. Equivalent values for Ni (Table 5) were taken from the work of Jaksic et al. [37]. The exchange current density and transfer coefficient for oxygen reduction (Table 1) were taken from Yu et al. [46], who measured the values for 60 °C and 25 °C. The reference concentration of oxygen was assumed to be equal to the inlet value, which was based on air at 1 bar and 25 °C in the default case (Table 2).

The volume fractions of catalyst in the anode and CCLs (Table 3) can be found from:

$$\varepsilon_{\text{M,a}} = \frac{m_{\text{M,a}}}{\rho_{\text{M}} l_{\text{acl}}} \quad \text{and} \quad \varepsilon_{\text{Pt,c}} = \frac{m_{\text{Pt,c}}}{\rho_{\text{Pt}} l_{\text{ccl}}} \quad (40)$$

respectively, where $m_{\text{M,a}}$ and $m_{\text{Pt,c}}$ are the anode catalyst and cathode Pt loadings (kg per m^2 of the anode geometric surface area), respectively. ρ_{M} and ρ_{Pt} are the densities of the anode catalyst

Table 4

Default mass- and charge-transport properties used in the model.

Symbol	Quantity	Value	Reference
$D_{\text{BH}_4^-}$	Diffusion coefficient of BH_4^- in anolyte (2 M NaOH)	$1.0 \times 10^{-5} \text{ cm}^2 \text{ s}^{-1}$	[28]
$D_{\text{BO}_2^-}$	Diffusion coefficient of BO_2^- in anolyte	$2.24 \times 10^{-5} \text{ cm}^2 \text{ s}^{-1}$	[29]
D_{OH^-}	Diffusion coefficient of OH^- in anolyte (2 M NaOH)	$8.2 \times 10^{-6} \text{ cm}^2 \text{ s}^{-1}$	[60]
D_{Na^+}	Diffusion coefficient of Na^+ in anolyte (2 M NaOH)	$5.5 \times 10^{-6} \text{ cm}^2 \text{ s}^{-1}$	[60]
D_{O_2}	Diffusion coefficient of O_2 in GDL (in air @ STP)	$0.21 \text{ cm}^2 \text{ s}^{-1}$	[29]
D_f	Diffusion coefficient of O_2 through diffusion film layer (Nafion) in the cathode	$5.9 \times 10^{-7} \text{ cm}^2 \text{ s}^{-1}$	[61]
$\sigma_{\text{GDL}}^{\text{eff}}$	Effective conductivity of cathode GDL	12.5 S cm^{-1}	[58]
K	Constant in equation (26)	$0.5 \text{ m}^{1/2}$	Assumed ^a

^a See Section 2.6.**Table 5**

Rate constants for a cell using a Ni/C anode catalyst. All other parameter values are as given in Tables 1–4.

Symbol	Quantity	Value	Reference
a_1	Charge transfer coefficient for reaction (4)	0.5	Assumed ^a
a_2	Charge transfer coefficients for reactions (3)	0.5	[40]
$j_{\text{BH,ref}}$	Reference exchange current density for reaction (4)	0.6 A m^{-2}	[45]
$\overleftarrow{k}_{\text{V}}$	Backward rate constant for Volmer reaction (3)	$6 \times 10^{-5} \text{ mol m}^2 \text{ s}^{-1}$	[37]
$\overrightarrow{k}_{\text{V}}$	Forward rate constant for Volmer reaction (3)	$5 \times 10^{-6} \text{ mol m}^2 \text{ s}^{-1}$	[37]
$\overleftarrow{k}_{\text{H}}$	Backward rate constant for Heyrovsky reaction (3)	$4.2 \times 10^{-8} \text{ mol m}^2 \text{ s}^{-1}$	[37]
$\overrightarrow{k}_{\text{H}}$	Forward rate constant for Heyrovsky reaction (3)	$1.5 \times 10^{-7} \text{ mol m}^2 \text{ s}^{-1}$	[37]
$\overleftarrow{k}_{\text{T}}$	Backward rate constant for Tafel reaction (3)	$7.8 \times 10^{-8} \text{ mol m}^2 \text{ s}^{-1}$	[37]
$\overrightarrow{k}_{\text{T}}$	Forward rate constant for Tafel reaction (3)	$1.3 \times 10^{-5} \text{ mol m}^2 \text{ s}^{-1}$	[37]
$\overleftarrow{k}_{\text{BH}}$	Backward rate constant for reaction (5)	$0 \text{ mol m}^2 \text{ s}^{-1}$	[8]
$\overrightarrow{k}_{\text{BH}}$	Forward rate constant for reaction (5)	$1 \times 10^{-6} \text{ mol m}^2 \text{ s}^{-1}$	Fitted
r_a	Roughness factor of the anode	100	Assumed ^a
$m_{\text{Ni,a}}$	Ni loading in the anode catalyst layer	40 g m^{-2}	Assumed ^a

^a See Section 2.6.

and cathode Pt, respectively. The default loadings in Table 1, both based on Pt, were taken to be 0.4 mg cm^{-2} and 4 mg cm^{-2} for the cathode and anode, respectively, both with 40% catalyst-to-carbon wt.% (these values are typical of unit DBFCs).

The adjustable (fitted) parameters are listed below.

1. The reaction constants $\overrightarrow{k}_{\text{BH}}$ and $\overleftarrow{k}_{\text{BH}}$ in equation (6). Following Chatenet et al. [8], the backward constant, representing desorption is considered zero, i.e., adsorption is irreversible. The selected value of $\overrightarrow{k}_{\text{BH}}$ (Table 1) will be discussed in the next section.
2. The boundary layer thickness in the anode is specified by the value of the constant K in equation (26). The value of K is system specific and is not available. The selected value of K (Table 4) will again be discussed in the next section.
3. The Na^+ conductivity of the Nafion® type membrane depends on the membrane water content and the temperature but the precise nature of the dependence has not been characterized. The conductivity also depends on the concentration of the NaOH in the anolyte to which the membrane is exposed on the anode side. The results of Narębska et al. [42] suggest a Nafion® 120 conductivity value of between 1 and 2.5 S m^{-1} for NaOH concentrations in the range 0.1–2 M in aqueous solution at 298 K. Ma et al. [47] measured the conductivity of a Nafion® 212 membrane equilibrated with 10 wt.% aqueous NaOH solution at room temperature and recorded a value of 0.74 S m^{-1} . A value of 0.5 S m^{-1} (Table 4) was chosen as the default value and the effects of deviations from this value were investigated, as detailed in the next section.

3. Results and discussion

3.1. Performance using a platinum anode catalyst

Simulations were performed using the default values in Tables 1–4 and the results are depicted in Figs. 3–5 (the term

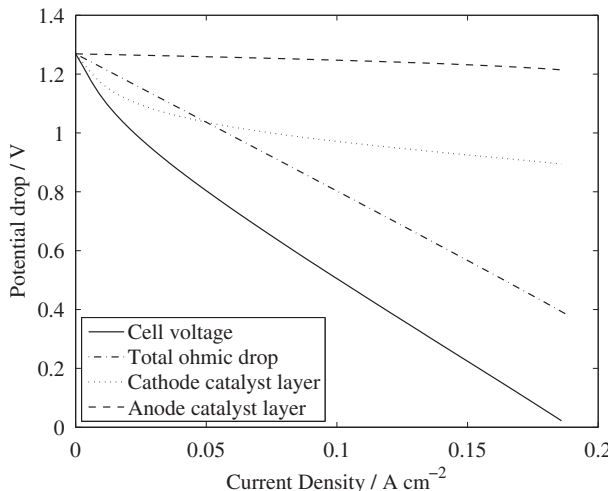


Fig. 3. The cell voltage and the individual component of the total voltage loss vs. the applied (total) current density for the base-case parameters in Tables 1–4. The anode catalyst is Pt/C.

'Current density' on the x -axis of all figures refers to the applied (total) current density). Fig. 3 shows the cell voltage at different applied current densities, along with the individual components of the voltage loss. This figure clearly indicates that the ohmic losses represent a significant portion of the total losses, which is consistent with experimental observations for both O_2 and H_2O_2 systems, e.g., [48–50]. The ohmic losses are dominated by the resistance to ion transport in the membrane, the ionomers and the electrolyte solution, as discussed later. Another notable feature of Fig. 3 is the relatively small anode polarization (deviation of the mixed anode potential from the anode mixed open-circuit potential), particularly in comparison to the cathode activation/mass-transport losses. This is again consistent with a number of experimental observations [4,48,50]; the reference exchange current densities for borohydride oxidation (Table 1) and hydrogen evolution ($\sim 10^{-4} \text{ A m}^{-2}$ in NaOH at room temperature [40]) on Pt are much higher than the reference exchange current density for oxygen reduction on Pt (Table 1), which partly explains these observations. It should be pointed out that the OCV in Fig. 3 is between 0.2 and 0.1 V higher than is typically found for DBFC employing Pt/C anodes [6,7]. This discrepancy is probably due to borohydride crossover to the cathode (particularly at low current densities) and the establishment of a mixed cathode potential [20,21], which is not incorporated in the model.

The current densities associated with direct borohydride oxidation (4) and hydrogen evolution/oxidation (3) are shown in Fig. 4, together with the mixed anode potential and mixed anode open-circuit potential. The borohydride current density (equal in magnitude to the hydrogen evolution current density at the OCV) is non-zero at the OCV (Fig. 4(a)), leading to the establishment of a mixed potential, E_{mixed} of around -0.87 V (Fig. 4(b)). This potential is considerably more positive than the standard potential for reaction (4), as is invariably the case in practice. At an applied current density of around 125 mA cm^{-2} , the borohydride and hydrogen current densities are equal and above this value of the applied current density the hydrogen oxidation current density is actually higher than the borohydride oxidation current density. It is interesting to note that in this case (i.e., for the given kinetic parameters) the borohydride current density remains almost constant as the applied current is increased. The sum of the two current densities (referred to the same geometric area) must equal the total applied current density; the applied and hydrogen current densities differ approximately by a constant value, which represents the borohydride current.

The mixed open-circuit anode potential, E_{mixed}^0 is also shown in Fig. 4(b). This value represents the potential at which the net current is zero. As the current density is increased, the mixed open-circuit potential increases, reflecting the changes in the BH_4^- surface concentration and the adsorbed species coverages at steady state. The latter are shown in Fig. 5. The surface coverage of hydrogen is around 0.27 under open-circuit conditions (Fig. 5(a)), while the coverage of BH_4^- is considerably lower. This result was robust to order-of-magnitude changes in the value of the reaction constant k_{BH} for the given values of the hydrogen evolution kinetic constants and the borohydride exchange current density. Outside this range of values for the adsorption constant k_{BH} , the results were not physically meaningful (given the highly nonlinear nature of the kinetic model, it is not surprising that the character of the solutions is sensitive to changes in the kinetic parameters). The results suggest, therefore, that only a small surface coverage of BH_4^- is required to sustain the borohydride oxidation reaction, given the higher overpotential for reaction (4), η_{BH} , compared to that for reaction (3), η_H . At a zero current density, the BH_4^- surface concentration (Fig. 5(b)) is appreciably lower than the inlet value, as a result of the high borohydride current density (BH_4^- consumption) under open-circuit conditions (Fig. 4(a)).

Fig. 6 illustrates the relationships between the applied current density and (a) the cell voltage and (b) the hydrogen evolution/oxidation current densities for different BH_4^- concentrations. The

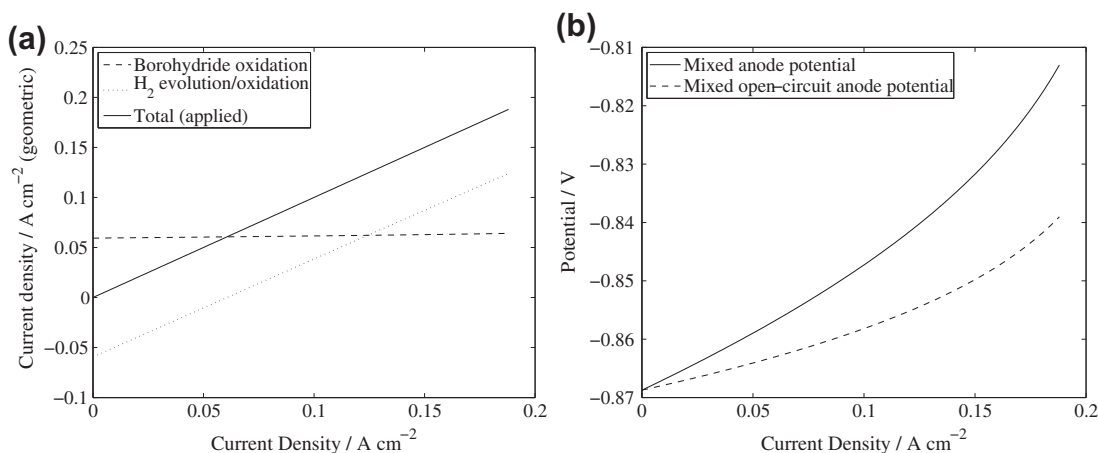


Fig. 4. (a) The borohydride and hydrogen currents and (b) the mixed anode potentials vs. the applied (total) current density for the base-case parameters in Tables 1–4. The anode catalyst is Pt/C.

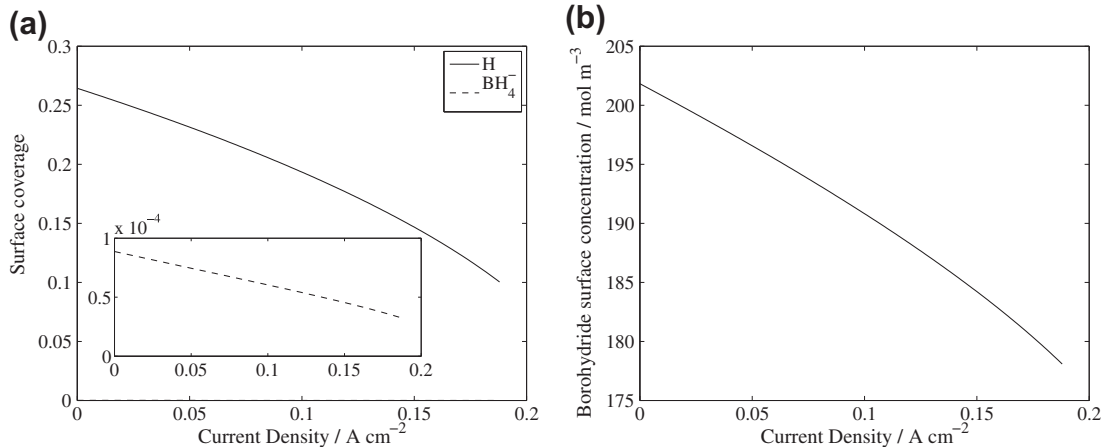


Fig. 5. (a) The borohydride ion and hydrogen adatom surface coverages and (b) the borohydride ion surface concentration vs. the applied (total) current density for the base-case parameters in Tables 1–4. The anode catalyst is Pt/C.

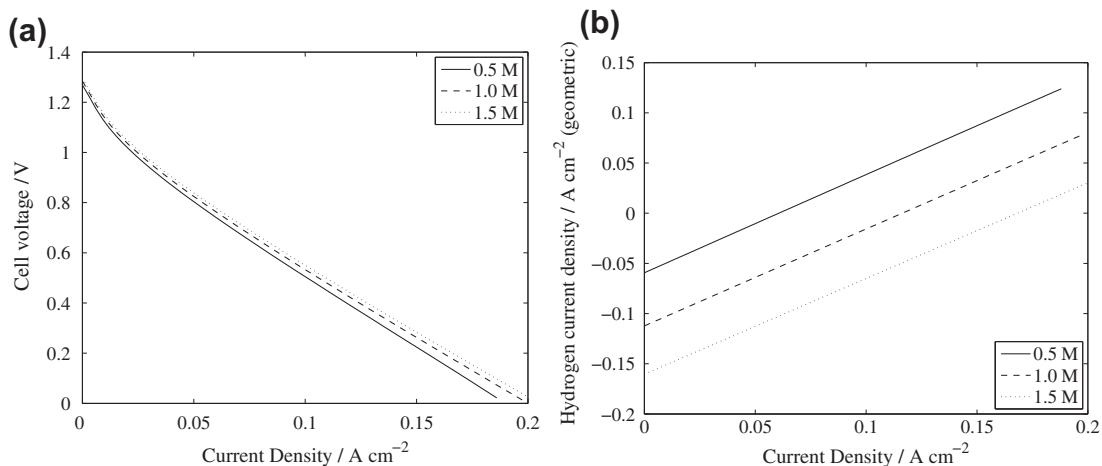


Fig. 6. The effect of varying the borohydride ion concentration (in 2 M NaOH) on (a) the cell voltage and (b) the hydrogen evolution/oxidation current density (expressed per unit geometric area of the electrode) vs. the applied (total) current density. The other parameter values are given in Tables 1–4. The anode catalyst is Pt/C.

performance improves as the concentration is increased (Fig. 6(a)), which has been observed consistently in experimental cell studies on different catalysts, including Pt [21,32,33,51–53]. As the borohydride ion concentration is increased, the magnitude of the hydrogen evolution current under open-circuit conditions increases (Fig. 6(b)). This is caused by an increase in the surface coverage of BH₄⁻ (by a factor of approximately 5 when the BH₄⁻ concentration is increased from 0.5 M to 1.5 M), while the change in the mixed anode potential is small (approximately 0.02 V more negative at the OCV between 0.5 M and 1.5 M). At low current densities, the performance is often observed to deteriorate as the BH₄⁻ concentration is increased [51]. Under these conditions, the rate of BH₄⁻ crossover increases, which lowers the (mixed) potential in the cathode. This phenomenon is not, however, included in the model.

Fig. 7 shows the cell voltage and anode polarization for different anolyte flow rates. It is well known that increasing the flow rate (within a practical range) can provide relatively small improvements in performance [11,15,21,52], precisely as shown in Fig. 7. At a fixed current density, a faster flow rate ensures a higher concentration of the BH₄⁻ ions in the anode, which lowers the anode polarization. The latter result, shown in Fig. 7, agrees with the anode polarization measurements taken by Duteanu et al. [21].

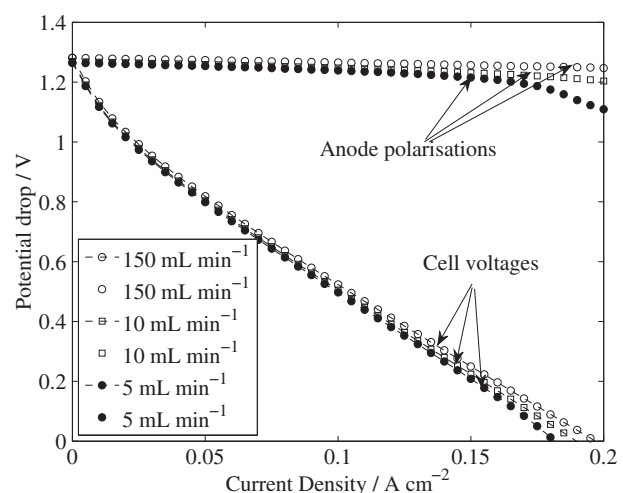


Fig. 7. The effect of varying the anolyte flow rate on the cell voltage and the anode polarization vs. the applied (total) current density. The other parameter values are given in Tables 1–4. The anode catalyst is Pt/C.

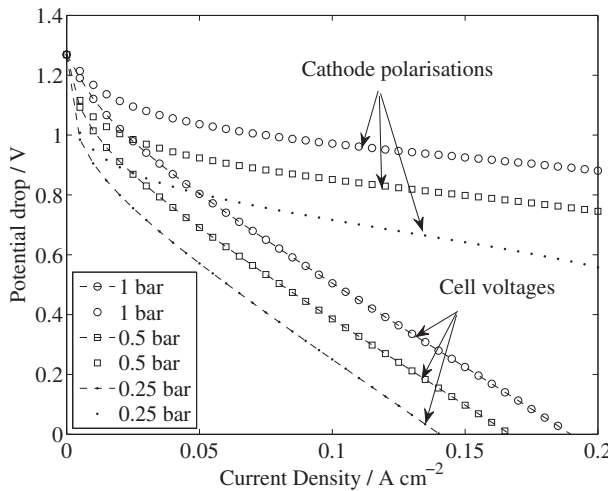


Fig. 8. The effect of varying the O_2 concentration (pressure) on the cell voltage and the cathode polarization vs. the applied (total) current density. The other parameter values are given in Tables 1–4. The anode and cathode catalysts are Pt/C.

Varying the oxygen concentration in the cathode inlet stream can have a greater impact on DBFC performance than varying either the flow rate or the BH_4^- concentration (within practical ranges) [11,52]. Fig. 8 shows the cell voltage curves and combined cathode activation/mass-transport losses for cathode air pressures of 1, 0.5 and 0.25 bar (assuming 21% O_2 by volume). There is a significant improvement in performance between the highest and lowest pressures; the peak power density is around 65% higher for 1 bar (the peak power density is attained at 95 mA cm^{-2} for 1 bar and at 69 mA cm^{-2} for 0.25 bar). The same degree of improvement (ca. 65%) was recorded by Celic et al. [51] when air was replaced with pure O_2 , i.e., a factor of five increase in the concentration of O_2 . This enhanced performance is due to improved mass transport to the catalyst sites through the diffusion boundary layer in the CCL (ionomer), leading to a higher surface concentration of O_2 . The effect of the higher surface concentration on the cathode overpotential at a fixed current density, which is the main factor in the performance improvement, is evident from Fig. 8.

It is worthwhile examining the individual components of the ohmic losses, the most significant of which are shown in Fig. 9(a) for the base-case parameters in Tables 1–4. The losses through the electron conducting components are small and are not, therefore,

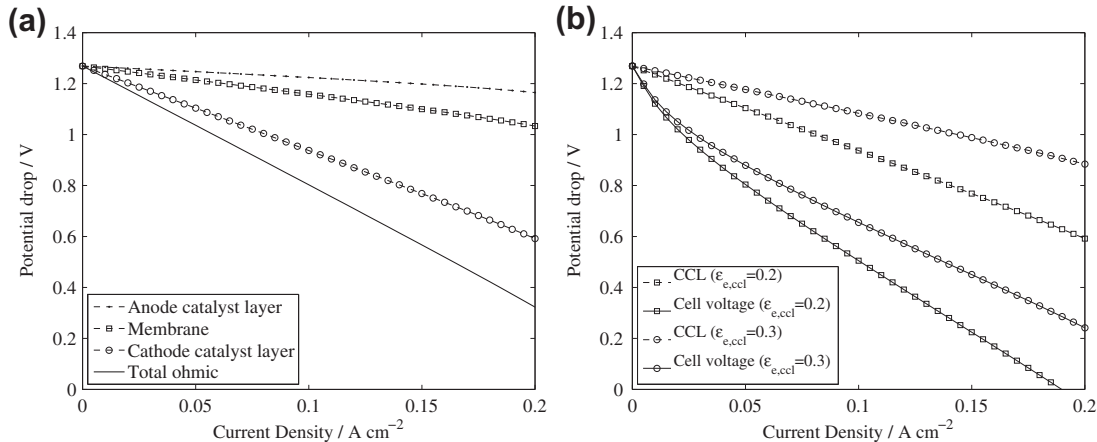


Fig. 9. (a) The main components of the total ohmic losses vs. the applied (total) current density based on the parameter values given in Tables 1–4. The anode catalyst is Pt/C. Losses through the electron conducting components were small and are not included. (b) The effect on the voltage drops vs. the applied (total) current density of increasing the CCL ionomer volume fraction to 0.3, with all other parameters fixed.

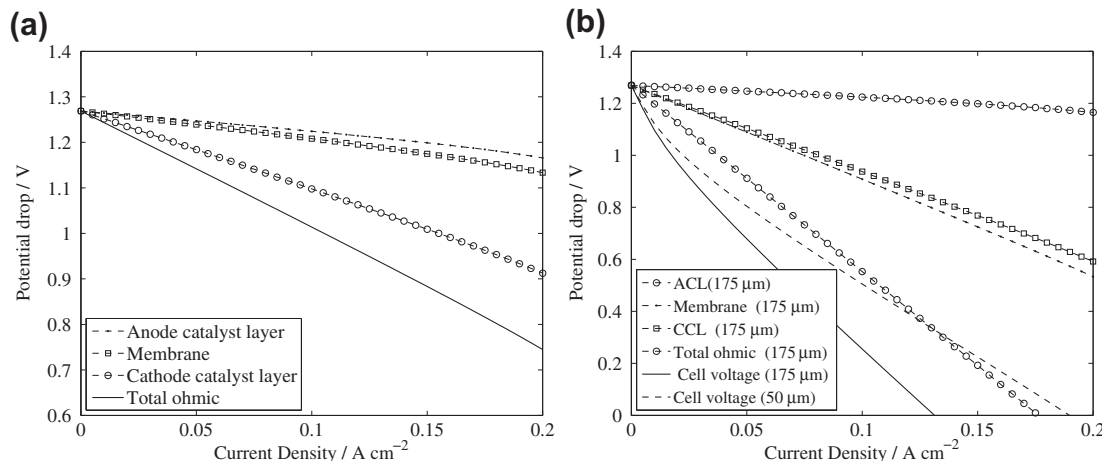


Fig. 10. A breakdown of the major ohmic losses according to cell component vs. the applied (total) current density for (a) a membrane conductivity of 1 S m^{-1} and (b) a membrane width of $175\text{ }\mu\text{m}$, with all other parameters as in Tables 1–4 in each case. The anode catalyst is Pt/C.

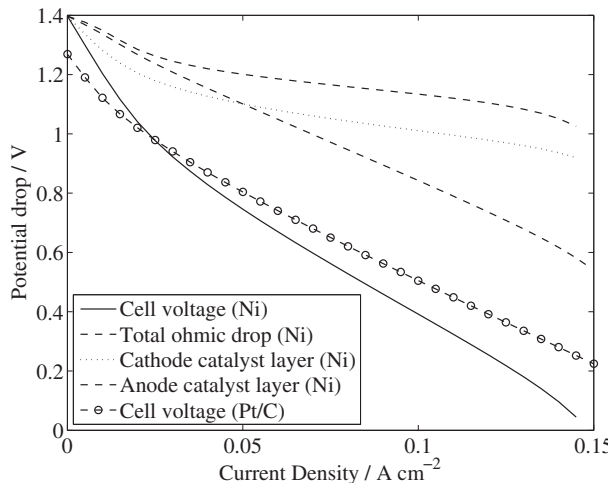


Fig. 11. The cell voltage and the individual component of the total voltage loss vs. the applied (total) current density in the case of a Ni/C anode catalyst. The parameter values are as in Tables 1–4 unless otherwise specified in the text.

included in this figure. For the given diffusion coefficients and inlet concentrations, the ionic conductivity of the anolyte is around 10 S m^{-1} , while the membrane/ionomer conductivity was assumed to take a value of 0.5 S m^{-1} . Therefore, for the given volume fractions in Table 3, the effective ACL ionic conductivity, $\sigma_{e,acl}^{\text{eff}}$, defined in equation (32), is approximately equal to the effective anolyte conductivity, also given in equation (32). The ACL losses are relatively small compared to the equivalent losses in the CCL, which is a consequence of the parallel pathways for ion migration in the ACL and the high solution conductivity in comparison to the ionomer conductivity. The CCL losses are strongly influenced by the volume of ionomer, and can be reduced significantly by increasing this volume fraction, without noticeably increasing the mass-transport resistance in the cathode, as demonstrated in Fig. 9(b).

The conductivity of the membrane is an important parameter of the cell and can be altered, at a fixed temperature, by the NaOH and water concentrations in the anolyte (to which the membrane is exposed on the anode side) and the relative humidity of the air (to which the membrane is exposed on the cathode side) [11]. The type of membrane/ionomer also influences the performance. For example, Ma et al. demonstrated a substantial uplift in performance by replacing a Nafion® 212 membrane/ionomer pair with a cross-linked chitosan membrane (CCS) in combination with a chitosan

chemical hydrogel as the anode binder; the conductivity of the CCS equilibrated with 10% aqueous NaOH at room temperature was recorded 11 S m^{-1} , compared to 0.74 S m^{-1} for the Nafion® 212 membrane. Fig. 10(a) shows the predicted ohmic losses when the membrane and ionomer conductivities are increased from 0.5 S m^{-1} to just 1 S m^{-1} , with all other parameters as in Tables 1–4. Both the membrane and CCL losses are halved, the latter of which leads to a dramatic reduction in the total ohmic losses (given the small volume of ionomer in the CCL), with an equal reduction in the total voltage losses.

Significant variations in performance have been observed between cells employing different Nafion® membranes [48,53]. The ohmic loss breakdown in Fig. 10(b) shows that an increase in the membrane thickness from $50 \mu\text{m}$ to $175 \mu\text{m}$ dramatically increases the membrane losses (the peak power density decreases by 29%). The thickness values of $50 \mu\text{m}$ and $175 \mu\text{m}$ correspond to the dry thicknesses of Nafion® 112 (or 212) and Nafion® 117, respectively, both of which were studied by Liu et al. [48]. The authors' results showed that the peak power density decreased by 14% when Nafion® 112 was replaced with Nafion® 117, which is roughly 50% of the value predicted by the model. If, on the other hand, the membrane/ionomer conductivity is increased to 1 S m^{-1} , the agreement is extremely good (both around 14% decrease with Nafion® 117). These results suggest that the marked difference in performance between cells employing different Nafion® membranes is largely a result of their different thicknesses, rather than any major differences in their ion transport properties.

3.2. Performance using a nickel anode catalyst

To simulate the performance when Ni is used as the anode catalyst, the values for the rate constants listed in Table 5 were used, while other parameter values were as given in Tables 1–4. A value of the exchange current density for the borohydride oxidation reaction on Ni, $j_{BH,\text{ref}}$ is not available from the literature. Cyclic voltammetry results [54,55] suggest that the exchange current density is significantly lower than that on Pt/C; Çelikkan et al. concluded that the activity of Ni towards borohydride oxidation is extremely limited. The value in Table 1 was, therefore, divided by an arbitrary factor k , which was varied between 1 and 10^6 . It was found that the character of the solutions did not change within this range; the differences were seen in the OCV and the H surface coverage at OCV, and will be discussed below. The results depicted in Figs. 11–13 are based on a value of $k = 1000$. Likewise, the unknown adsorption constant for reaction (5), \overrightarrow{k}_{BH} was arbitrarily chosen as

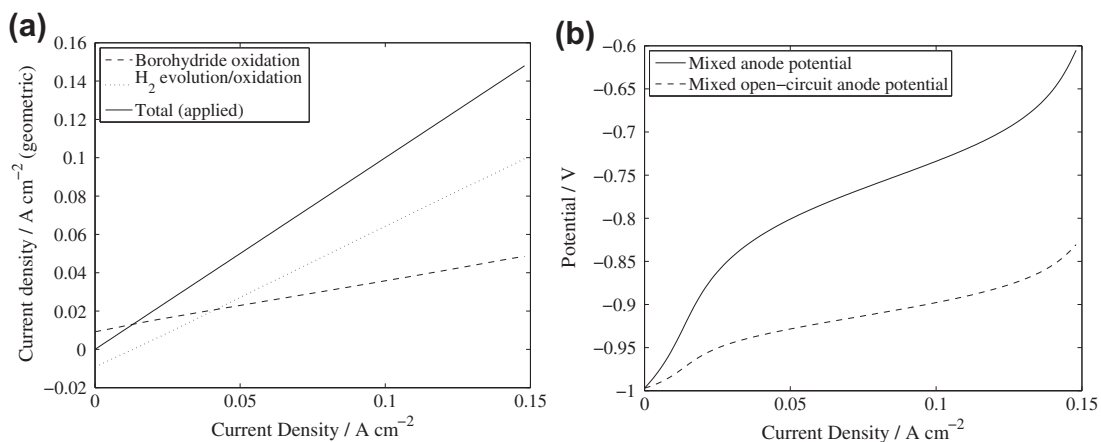


Fig. 12. (a) The borohydride and hydrogen currents and (b) the mixed anode potentials vs. the applied (total) current density in the case of a Ni/C anode catalyst. The parameter values are as in Tables 1–4 unless otherwise specified in the text.

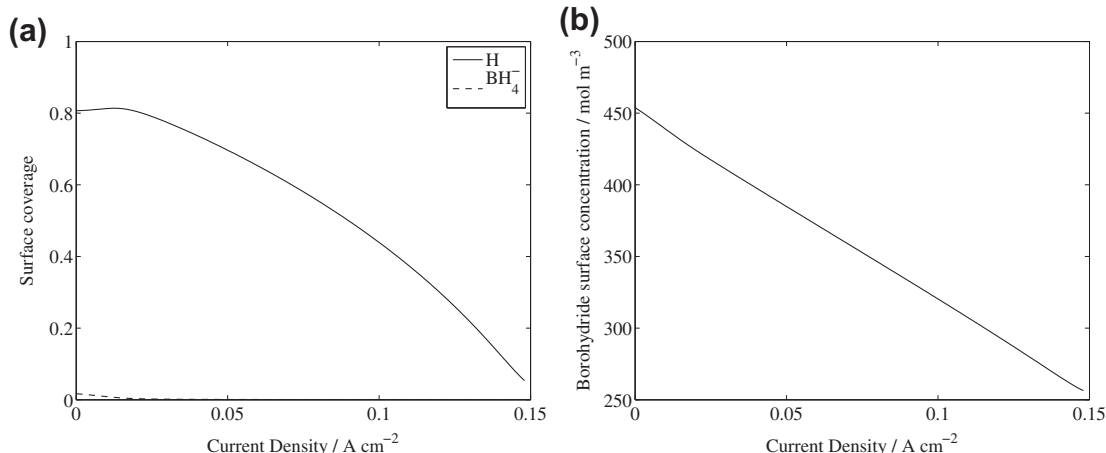


Fig. 13. (a) The borohydride ion and hydrogen adatom surface coverages and (b) the borohydride ion and hydrogen molecule surface concentrations vs. the applied (total) current density in the case of a Ni/C anode catalyst. The parameter values are as in Tables 1–4 unless otherwise specified in the text.

one-tenth of the value for Pt/C in Table 1. This parameter was also varied as discussed below.

Fig. 11 shows the cell voltage at different applied current densities and the individual components of the voltage loss for the Ni anode cell. The equivalent cell voltage curve for Pt/C (taken from Fig. 3) is included for comparison. Comparing the cell voltage curves for Ni and Pt/C shows that on Ni the OCV is around 0.13 V higher, while the limiting current density at 0 V is around 45 mA cm⁻² lower. There are few direct comparisons between Ni and Pt electrodes. Wang et al. [33] found a difference of around 0.13 V in the OCV between Ni powder and 20 wt.% Pt/C anodes (at 296 K and with 0.5 M NaBH₄), with a higher value when Ni was used. Liu et al. [56] recorded a difference of around 0.17 V (at 303 K and with 0.52 M NaBH₄), with the higher value again for Ni powder vs. 5 wt.% Pt/C. Cheng et al. [55], on the other hand, found that the OCV obtained with 42 wt.% carbon-supported Ni was approximately 0.03 V lower than on 43 wt.% Pt/C. The authors also found that the peak power density with Ni/C was 21% lower than for Pt/C, which compares to an equivalent decrease of 17% in the case depicted in Fig. 11. Neither Wang et al. nor Liu et al. generated full polarization curves, so comparisons cannot be made to their data. A discussion on the aforementioned trends is postponed until other aspects of the simulation results are discussed.

Fig. 12 shows the borohydride and hydrogen current densities and the mixed anode potential for the Ni anode. Comparing this figure with Fig. 4 reveals that the hydrogen evolution current density at the OCV is substantially lower for the Ni anode (Fig. 12(a)) and, correspondingly, the mixed anode potential is more negative (Fig. 12(b)), which leads to the higher OCV. As is evident from the rate constants in Tables 1 and 5, Ni is less active than Pt/C towards hydrogen evolution and borohydride oxidation. Both the borohydride and hydrogen current densities at the OCV are, therefore, lower than for Pt/C. The surface coverages of both H and BH₄⁻ at the OCV, shown in Fig. 13(a), are higher than the coverages on Pt/C in Fig. 4(a). These increases result from the slower borohydride and hydrogen reactions on Ni.

The direction in which the mixed anode potential at the OCV moves (towards E_{BH}⁰ or E_H⁰) as the reaction constants are varied depends on the relative sizes of the exchange current densities for the borohydride and hydrogen reactions. As j_{BH,ref} is decreased (with all other parameters fixed) by increasing the fitting parameter *k*, the mixed potential at a fixed current density moves closer to the standard potential for hydrogen evolution/oxidation. The borohydride overpotential η_{BH} increases in order to maintain

a balance between the hydrogen and borohydride current densities (see equations (16) and (18)), which leads to a smaller hydrogen overpotential η_H (the mixed anode potential is less negative) and concomitantly a smaller hydrogen evolution current density. The lower cell voltage values lead to a lower peak power density. For *k* = 2 × 10⁴, the OCV is approximately 0.02 V higher and the peak power density is approximately 21% lower than on Pt/C, which is very close to the result of Cheng et al. for a cell employing Ni/C [55]. The differences between the results of Wang et al. and Liu et al. [33,56] and those of Cheng et al. [55] could, therefore, be explained by the different exchange current densities for the Ni/C and the Ni-powder catalysts used.

The adsorption constant for reaction (5), \vec{k}_{BH} was arbitrarily chosen for the Ni simulation. Decreasing the value of \vec{k}_{BH} was found to decrease the cell voltage at a fixed current density by virtue of a lower surface coverage of BH₄⁻, requiring a larger overpotential for borohydride oxidation, η_{BH} in order to maintain charge conservation (equal borohydride and hydrogen current densities). The resultant decrease in the hydrogen overpotential, η_H decreases the hydrogen evolution current density. The basic character of the solutions (as described above) is not altered unless values of \vec{k}_{BH} smaller than 4 × 10⁻⁷ mol m² s⁻¹ are used, in which case the borohydride surface coverage is limiting. The surface concentration of BH₄⁻ reaches a limiting value, along with the borohydride and hydrogen overpotentials, leading to a characteristic bend in the polarization curve. There is no concrete example of such behaviour in the literature, so these low values of \vec{k}_{BH} were not considered to be physically meaningful.

4. Conclusions

In this paper, a framework for the detailed modelling of direct borohydride fuel cells has been developed. Comparisons to experimental data from the open literature have demonstrated that the model is able to capture the correct qualitative trends with respect to variations in several key parameters, including the fuel and oxidant concentrations and the membrane properties. A comparison between the simulated performance for Pt and Ni anode catalyst cells has revealed a number of key differences. These differences were explained in the context of the trends that have been observed in experimental studies. It appears that the hydrogen evolution (water reduction) current on Ni is considerably lower at the OCV (given the lower activity of Ni towards this reaction), with a correspondingly more

negative mixed anode potential, which ultimately leads to a higher OCV. The results also suggest that the OCV decreases as the exchange current density for borohydride oxidation decreases, which may explain the differences between Ni-powder and Ni/C catalysts.

The anode mechanism is highly complex; it depends on the concentration of sodium borohydride, the concentration of the alkali salt (NaOH or KOH typically), the temperature and the catalyst. The anode kinetic mechanism adopted in this paper incorporates borohydride oxidation, hydrogen evolution through hydrolysis, hydrogen evolution through water reduction and hydrogen oxidation. The role of intermediates such as $\text{BH}_3(\text{OH})^-$ and the adsorption of OH^- may, on the other hand, play important roles. It is important, therefore, to develop this aspect of the model further, which requires values for the rate constants pertaining to the various reaction mechanisms proposed in the literature (for each catalyst materials of interest).

Other important parameters that have not been measured systematically relate to the transport of species in the anolyte and the transport of Na^+ in the membrane. The simulations confirm that ohmic losses represent a considerable portion of the total cell losses. The Na^+ conductivities of the perfluorosulfonic-acid and other ion-exchange membranes used in DBFCs depend on the operating environment. The conductivity values can vary significantly between membrane types and between operating conditions. In order to fully exploit models for design and characterisation, it is particularly important to develop relationships between the Na^+ conductivity and the membrane water content/temperature of the environment.

The aim of this work was to develop a first detailed model of a DBFC. Aspects for consideration in extending the present model include spatial variations in the reactant concentrations and potentials, heat management and dynamic performance. The framework developed allows these aspects of performance to be incorporated in a relatively straightforward manner.

Appendix

Charge conservation and electrical neutrality in the catalyst layers demand that the electronic and ionic current densities, j_s and j_e , satisfy (neglecting double layer effects):

$$\frac{d}{dx}(j_e + j_s) = 0 \quad (\text{A1})$$

Integrating this equation and applying the boundary condition at either the membrane/catalyst-layer interface (zero electronic current density) or the diffusion-layer/catalyst-layer interface (zero ionic current density) yields:

$$j_e + j_s = j_{\text{applied}} \quad (\text{A2})$$

The total (applied) current density (referred to the geometric surface area of the electrode) is shared between the electronic and ionic conducting phases. The individual components j_e and j_s are given in terms of the potentials ϕ_e and ϕ_s by ohm's law, as in equations (33)–(36). They can also be related to the transfer (Faradaic) current densities, j_f in the electrodes by the following charge balances (consistent with equation (A1)) [22]:

$$\sigma_e \frac{d^2 \phi_e}{dx^2} = -\sigma_s \frac{d^2 \phi_s}{dx^2} = sj_f \quad (\text{A3})$$

where σ_s and σ_e are the relevant effective electronic and ionic conductivities and s is the specific surface area of the electrode (active surface area per unit volume). The transfer current density is given by j_{O_2} in the CCL and by $j_{\text{BH}} + j_V + j_H$ in the ACL (equations (15)

and (17)). From their definitions, the specific surface area can be related to the roughness factor, r , and the thickness of the catalyst layer, l , as $s = r/l$. Therefore:

$$\sigma_e \frac{d^2 \phi_e}{dx^2} = -\sigma_s \frac{d^2 \phi_s}{dx^2} = \frac{j_{\text{applied}}}{l} \quad (\text{A4})$$

Integrating the second of these equations twice from the liquid diffusion layer/ACL interface, $x = x_1$, to some arbitrary x in the ACL, applying the boundary condition $\sigma_s(d\phi_s/dx) = j_{\text{applied}}$ at $x = x_1$, yields:

$$j_s = \sigma_s \frac{d\phi_s}{dx} = \frac{(l - (x - x_1))}{l} j_{\text{applied}} \quad (\text{A5})$$

The average value of j_s is found by integrating the right hand side of equation (A5) w.r.t. x between $x = x_1$ and the membrane/ACL interface, $x = x_2$, which gives a value of $j_{\text{applied}}/2$, as used in the formulae in Section 2.4. Integrating equation (A5) across the ACL yields the equivalent formula:

$$\Delta\phi = \phi(x_2) - \phi(x_1) = \frac{l j_{\text{applied}}}{2\sigma_s} \quad (\text{A6})$$

This analysis can be extended to the ionic potential in the ACL and to the electronic and ionic potentials in the CCL.

References

- [1] J. Laramie, A. Dicks, Fuel Cell Systems Explained, second ed. Wiley & Sons, New York, 2003.
- [2] A.K. Shukla, C.L. Jackson, K. Scott, Bull. Mater. Sci. 26 (2003) 207–214.
- [3] S.C. Amendola, P. Onnerud, M.T. Kelly, P.J. Petillo, S.L. Sharp-Goldman, M. Binder, J. Power Sources 84 (1999) 130–133.
- [4] Z.P. Li, B.H. Liu, K. Arai, S. Suda, J. Electrochem. Soc. 150 (2003) 868–872.
- [5] C. Ponce de León, F.C. Walsh, A. Rose, J.B. Lakeman, D.J. Browning, R.W. Reeve, J. Power Sources 164 (2007) 441–448.
- [6] C. Ponce de León, F.C. Walsh, D. Pletcher, D.J. Browning, J.B. Lakeman, J. Power Sources 155 (2006) 172–181.
- [7] J. Ma, N.A. Choudhury, Y. Sahai, Renew. Sustain. Energy Rev. 14 (2010) 183–199.
- [8] M. Chatenet, F. Micoud, I. Roche, E. Chainet, Electrochim. Acta 51 (2006) 5459–5467.
- [9] R.X. Feng, H. Dong, Y.D. Wang, X.P. Ai, Y.L. Cao, H.X. Yang, Electrochim. Commun. 7 (2005) 449–452.
- [10] U.B. Demirci, J. Power Sources 172 (2007) 676–687.
- [11] C. Celik, F.G. Boyaci San, H.I. Sarac, J. Power Sources 185 (2008) 197–201.
- [12] N.A. Choudhury, R.K. Raman, S. Sampath, A.K. Shukla, J. Power Sources 143 (2005) 1–8.
- [13] J.H. Kim, H.S. Kim, Y.M. Kang, M.S. Song, S. Rajendran, S.C. Han, D.H. Jung, J.Y. Lee, J. Electrochem. Soc. 151 (2004) 1039–1043.
- [14] Z.P. Li, B.H. Liu, J.K. Zhu, S. Suda, J. Power Sources 163 (2006) 555–559.
- [15] M.H. Atwan, C.L.B. Macdonald, D.O. Northwood, E.L. Gyenge, J. Power Sources 158 (2006) 36–44.
- [16] K.T. Park, U.H. Jung, S.U. Jeong, S.H. Kim, J. Power Sources 162 (2006) 192–197.
- [17] C. Ponce de León, A. Kulak, S. Williams, I. Merino-Jiménez, F.C. Walsh, Catal. Today 170 (2011) 148–154.
- [18] B.H. Liu, Z.P. Li, J. Power Sources 187 (2009) 291–297.
- [19] Z.P. Li, B.H. Liu, K. Arai, K. Asaba, S. Suda, J. Power Sources 126 (2004) 28–33.
- [20] B.H. Liu, S. Suda, J. Power Sources 164 (2007) 100–104.
- [21] N. Duteau, G. Vlachogiannopoulos, M.R. Shivhare, E.H. Yu, K. Scott, J. Appl. Electrochem. 37 (2007) 1085–1091.
- [22] A.A. Shah, K.H. Luo, T.R. Ralph, F.C. Walsh, Electrochim. Acta 56 (2011) 3731–3757.
- [23] I. Merino-Jiménez, C. Ponce de León, A.A. Shah, F.C. Walsh, J. Power Sources 219 (1) (2012) 339–357.
- [24] A. Verma, S. Basu, J. Power Sources 168 (2007) 200–210.
- [25] A.E. Sanli, M.L. Aksu, B.Z. Uysal, Int. J. Hydrogen Energy 36 (2011) 8542–8549.
- [26] A.A. Shah, H. Al-Fetlawi, F.C. Walsh, Electrochim. Acta 55 (2010) 1125–1139.
- [27] B.H. Liu, S. Suda, J. Alloys Compd. 454 (2008) 280–285.
- [28] E. Gyenge, Electrochim. Acta 49 (2004) 965–978.
- [29] M. Chatenet, M.B. Molina-Concha, N. El-Kissi, G. Parrou, J.P. Diard, Electrochim. Acta 54 (2009) 4426–4435.
- [30] M.V. Mirkin, A.J. Bard, Anal. Chem. 63 (1991) 532–533.
- [31] M.V. Mirkin, H. Jang, A.J. Bard, J. Electrochem. Soc. 139 (1992) 2212–2217.

- [32] K. Wang, J. Lu, L. Zhuang, *J. Phys. Chem. C* 111 (2007) 7456–7462.
- [33] K. Wang, J. Lu, L. Zhuang, *Catal. Today* 170 (2011) 99–109.
- [34] J. Newman, K.E. Thomas-Alyea, *Electrochemical Systems*, third ed., Wiley & Sons, New York, 2004.
- [35] H. Cheng, K. Scott, *Electrochim. Acta* 51 (2006) 3429–3433.
- [36] A. Lasia, A. Rami, *J. Electroanal. Chem.* 294 (1990) 123–141.
- [37] J.M. Jakšić, M.V. Vojnović, N.V. Krstajić, *Electrochim. Acta* 45 (2000) 4151–4158.
- [38] L. Bai, *J. Electroanal. Chem.* 355 (1993) 37–55.
- [39] M.R. Gennaro de Chialvo, A.C. Chialvo, *J. Electrochem. Soc.* 147 (2000) 1619–1622.
- [40] S.A. Vilekar, I. Fishtik, R. Datta, *J. Electrochem. Soc.* 157 (2010) B1040–B1050.
- [41] D. Pletcher, F.C. Walsh, *Industrial Electrochemistry*, second ed., Chapman and Hall, London, 1990.
- [42] D.A.G. Bruggeman, *Ann. Phys.* 24 (1935) 636–664.
- [43] C.V. Chrysikopoulos, P.Y. Hsuan, M.M. Fyrillas, K.Y. Lee, *J. Hazard. Mater.* B97 (2003) 245–255.
- [44] B. Molina-Concha, M. Chatenet, *Electrochim. Acta* 54 (2009) 6119–6129.
- [45] B. Molina-Concha, M. Chatenet, *Electrochim. Acta* 54 (2009) 6130–6139.
- [46] E.H. Yu, K. Scott, R.W. Reeve, *Fuel Cells* 3 (2003) 169–176.
- [47] J. Ma, N.A. Choudhury, Y. Sahai, R.G. Buchheit, *Electrochim. Acta* 196 (2011) 8257–8264.
- [48] B.H. Li, Z.P. Li, K. Arai, S. Suda, *Electrochim. Acta* 50 (2005) 3719–3725.
- [49] B.H. Liu, Z.P. Li, J.K. Zhu, S. Suda, *J. Power Sources* 183 (2008) 151–156.
- [50] R.K. Raman, A.K. Shukla, *Fuel Cells* 7 (2007) 225–231.
- [51] C. Celik, F.G. Boyaci San, H.I. Sarac, *J. Power Sources* 195 (2010) 2599–2603.
- [52] H. Cheng, K. Scott, *J. Power Sources* 160 (2006) 407–412.
- [53] W. Haijun, W. Cheng, L. Zhixiang, M. Zongqiang, *Int. J. Hydrogen Energy* 35 (2010) 2648–2651.
- [54] H. Celikkannan, M. Sahin, M.L. Aksu, T.N. Veziroglu, *Int. J. Hydrogen Energy* 32 (2007) 588–593.
- [55] H. Cheng, K. Scott, K. Lovell, *Fuel Cells* (2006) 367–375.
- [56] B.H. Liu, Z.P. Li, S. Suda, *Electrochim. Acta* 49 (2004) 3097–3105.
- [57] E.A. Ticianelli, C.R. Derouin, S. Srinivasan, *J. Electroanal. Chem.* 251 (1988) 275–295.
- [58] M. Mathias, J. Roth, J. Fleming, W. Lehnert, in: Wolf Vielstich, Hubert A. Gasteiger, A. Lamm (Eds.), *Handbook of Fuel Cells – Fundamentals, Technology and Applications*, John Wiley & Sons, 2003.
- [59] S. Litster, G. McLean, *J. Power Sources* 130 (2004) 61–76.
- [60] M. Zapalowski, W.M. Bartczak, *Comput. Chem.* 24 (2000) 450–468.
- [61] A.T. Haug, R.E. White, *J. Electrochem. Soc.* 147 (2000) 980–983.